Optimizing magneto-ionic performance in structure/composition-engineered ternary nitrides

Zheng Ma, P Monalisha, Zhengwei Tan, Eva Pellicer, Maciej O Liedke, Maik Butterling, Ahmed G Attallah, Eric Hirschmann, Andreas Wagner, Fatima Ibrahim, et al.

Journal of Materiomics 10 (2024) 870–879

Contents lists available at ScienceDirect

Journal of Materiomics

journal homepage: www.journals.elsevier.com/journal-of-materiomics/

Research paper

Optimizing magneto-ionic performance in structure/composition-engineered ternary nitrides

Zheng Ma [a, **], P. Monalisha [a], Zhengwei Tan [a], Eva Pellicer [a], Maciej O. Liedke [b], Maik Butterling [b], Ahmed G. Attallah [b], Eric Hirschmann [b], Andreas Wagner [b], Fatima Ibrahim [c], Mairbek Chshiev [c, d], Enric Menéndez [a, ***], Jordi Sort [a, e, *]

[a] Departament de Física, Universitat Autònoma de Barcelona, Cerdanyola del Vallès, 08193, Spain
[b] Institute of Radiation Physics, Helmholtz-Zentrum Dresden – Rossendorf, Dresden, 01328, Germany
[c] University of Grenoble Alpes, CEA, CNRS, SPINTEC, Grenoble, 38000, France
[d] Institut Universitaire de France, Paris, 75231, France
[e] Institució Catalana de Recerca i Estudis Avançats (ICREA), Pg. Lluís Companys 23, Barcelona, 08010, Spain

ARTICLE INFO

Article history:
Received 20 August 2023
Received in revised form
15 October 2023
Accepted 18 October 2023
Available online 4 November 2023

Keywords:
Voltage control of magnetism
Magneto-ionics
Electrolyte gating
Ternary nitrides
Ion transport

ABSTRACT

Magneto-ionics, an emerging approach to manipulate magnetism that relies on voltage-driven ion motion, holds the promise to boost energy efficiency in information technologies such as spintronic devices or future non-von Neumann computing architectures. For this purpose, stability, reversibility, endurance, and ion motion rates need to be synergistically optimized. Among various ions, nitrogen has demonstrated superior magneto-ionic performance compared to classical species such as oxygen or lithium. Here, we show that ternary $Co_{1-x}Fe_xN$ compound exhibits an unprecedented nitrogen magneto-ionic response. Partial substitution of Co by Fe in binary CoN is shown to be favorable in terms of generated magnetization, cyclability and ion motion rates. Specifically, the $Co_{0.35}Fe_{0.65}N$ films exhibit an induced saturation magnetization of 1,500 emu/cm^3, a magneto-ionic rate of 35.5 emu/(cm^3·s) and endurance exceeding 10^3 cycles. These values significantly surpass those of other existing nitride and oxide systems. This improvement can be attributed to the larger saturation magnetization of $Co_{0.35}Fe_{0.65}$ compared to individual Co and Fe, the nature and size of structural defects in as-grown films of different composition, and the dissimilar formation energies of Fe and Co with N in the various developed crystallographic structures.

1. Introduction

Manipulation of matter's magnetism is traditionally accomplished by applying magnetic fields or through spin-polarized currents. The use of other, non-magnetic stimuli, such as strain, [1,2] light [3,4] or voltage (*i.e.*, electric field) is highly appealing since it provides additional degrees of freedom to conventional materials' actuation protocols, eventually leading to enhanced functionalities that can be of interest in a myriad of technological applications. Voltage control of magnetism holds the potential to boost energy efficiency in low-power spintronic systems since energy dissipation by Joule heating effect might be strongly minimized compared to spin-transfer-torque devices [5–8]. Within this approach, magneto-ionics, *i.e.*, the modulation of magnetic properties by voltage-driven ionic motion, stands out from other converse magnetoelectric mechanisms due to its large and non-volatile modulation of magnetism with electric fields [9–11]. H^+, [12–15] Li^+ [16–18] and O^{2-} [19–23] are the most usual ions to be transported. Even though O^{2-} magneto-ionics is limited in terms of ion motion speed and cyclability (compared to H^+ and Li^+ based magneto-ionics), O^{2-} is still one of the most commonly investigated magneto-ionic ion species since its voltage-driven motion can be induced in a large variety of oxide materials with relatively high stability and robustness. Interestingly, while also preserving non-volatility, N^{3-} magneto-ionics has been shown favorable to

* Corresponding author. Departament de Física, Universitat Autònoma de Barcelona, Cerdanyola del Vallès, 08193, Spain.
** Corresponding author.
*** Corresponding author.
E-mail addresses: ma.zheng@uab.cat (Z. Ma), enric.menendez@uab.cat (E. Menéndez), jordi.sort@uab.cat (J. Sort).
Peer review under responsibility of The Chinese Ceramic Society.

https://doi.org/10.1016/j.jmat.2023.10.007

O^{2-} magneto-ionics as regards to ion motion rates and cyclability [24–28]. This was demonstrated by comparing the magneto-ionic response through voltage-driven O^{2-} and N^{3-} motion in Co_3O_4 and CoN films, respectively (both of them with cubic crystallographic structure and with the same thickness) [24]. Besides microstructure, where structural defects play a central role in voltage-driven ion transport, the faster response of N^{3-} compared to O^{2-} is ultimately linked to the lower electronegativity of nitrogen with the transition metal, which tends to result in weaker chemical bonds and, hence, lower cohesive energies. Recently, it has been shown that, by partially substituting Co in CoN with Mn, refined microstructures (with larger amounts of grain boundaries, probably stemming from the tendency to form competing crystallographic phases) and reduced cohesive energies can be achieved, resulting in enhanced N^{3-} motion and cyclability [27]. However, Mn is not ferromagnetic. This, besides being detrimental in terms of the attainable voltage-generated net magnetization, also limits the amount of Mn that can be incorporated in the ternary nitride compounds since Co–Mn alloys are ferromagnetic only for Mn contents lower than 25% (in mole) [29]. Therefore, the use of other ferromagnetic elements, such as Fe, may allow further exploitation of this multi-element transition-metal nitride engineering approach, since larger fractions of the substitutional element would be magneto-ionically available. Analogously to Mn, Fe has a body-centered cubic (bcc) crystal structure, whereas Co is either hexagonal-close packed (hcp) or face-centered cubic (fcc) when it is nanostructured. This might lead to a mixture of phases with complex microstructures, promoting the existence of large amounts of grain boundaries, which are favorable to ion diffusion compared to bulk migration. Furthermore, $Co_{1-x}Fe_x$ alloys with x ranging between 0.6 and 0.7 are known to exhibit the highest saturation magnetization reported so far [30,31].

In this work, we investigate the magneto-ionic response of $Co_{1-x}Fe_xN$ films as a function of the Fe content, x ($0 \leq x < 1$), by conducting in-plane magnetometry while gating the system using a liquid electrolyte to generate *in-situ* electric fields. Our results reveal that partial substitution of Co by Fe in CoN is favorable in terms of generated magnetization, ion motion rates and cyclability. Specifically, the voltage-treated $Co_{0.35}Fe_{0.65}N$ films exhibit an induced saturation magnetization of 1,500 emu/cm^3 (1 emu/cm^3 = 1,000 A/m), a nitrogen ion speed of 35.5 emu/(cm^3·s) and a cyclability above 10^3 cycles, being the largest values reported so far for nitrogen magneto-ionics. These outstanding results are linked to the larger saturation magnetization of $Co_{0.35}Fe_{0.65}$ compared to pure Co and Fe, the induced changes in the defect structure of the films (with large amounts of defects that promote fast ion motion rates), and the decrease of the transition-metal nitride formation energy upon addition of Fe, which results in CoFe–N bonds that are weaker than in CoN.

2. Experimental section

2.1. Sample preparation

50 nm thick $Co_{1-x}Fe_xN$ ($0 \leq x < 1$) films were grown by reactive magnetron co-sputtering at room temperature on top of [100]-oriented Si substrates, previously coated with a Ti (20 nm) and a Cu (60 nm) layers that serve as working electrode. An AJA International ATC 2400 sputtering system with a base pressure of around 5×10^{-8} Torr was used. The Si/Ti (20 nm)/Cu (60 nm) substrates were partially masked during deposition to allow making the electric contact to Cu during electrolyte gating. The target-to-substrate distance was around 11 cm. Reactive sputtering was done at a total pressure of 3×10^{-3} Torr in an Ar and N_2 mixed atmosphere. The Ar:N_2 flow ratio was set to 1:1 to provide a nitrogen-rich atmosphere needed for the growth of the non-ferromagnetic nitrides. A metallic Fe target source was operated at a constant DC power of 50 W, while the Co target was channeled to a RF source. The RF sputtering power was varied to achieve different Co:Fe ratios in the ternary nitride films. RF powers of 30, 50, 60, 80, 100 W and 120 W result in Fe contents, x, of 0.87, 0.75, 0.65, 0.51, 0.44 and 0.37, respectively, in $Co_{1-x}Fe_xN$, examined using a Zeiss MERLIN field-emission scanning electron microscope equipped with an Oxford INCA X-Max energy-dispersive spectroscopy detector (see Fig. S1, Supplementary Information). Binary CoN was RF-sputtered at an input power of 120 W. $Co_{0.35}Fe_{0.65}N$ films of 5, 10 nm and 25 nm were also grown using 50 W DC and 60 W RF sputtering powers, which give rise to deposition rates of around 0.5 Å/s.

2.2. Magnetoelectric measurements

Magnetoelectric measurements were performed using a vibrating sample magnetometer (VSM) from Micro Sense LOT-Quantum Design at room temperature while gating the films using a liquid electrolyte. Gating voltages were applied between the Cu working electrode and a Pt wire (acting as a counter electrode) in a capacitor-like configuration [21,24] using an external Agilent B2902A power supply. An anhydrous propylene carbonate (PC) with dissolved Na^+ (10–25 mg/L) and OH^- was used as the liquid electrolyte. Na^+ and OH^- arise from the reaction between water and metallic sodium, which is used to eliminate any traces of residual water in the PC [28]. Magnetic fields were applied along the film plane direction. Two types of measurements were performed: (i) standard magnetization *vs.* applied magnetic field hysteresis loops (lasting approximately 1 h each) and (ii) time-dependent magnetization measurements under an applied magnetic field of 10 kOe (1 kOe = 79.58 kA/m). Any linear contribution (*e.g.*, diamagnetic/paramagnetic signals from the sample holder or the Si substrate) was subtracted from the hysteresis loops.

2.3. Structural and compositional characterization

θ–2θ X-ray diffraction (XRD) patterns were recorded on a Materials Research Diffractometer from Malvern PANalytical using Cu K_α radiation. High-angle annular dark-field scanning transmission electron microscopy (HAADF-STEM), high-resolution transmission electron spectroscopy (HRTEM), and electron energy loss spectroscopy (EELS) were performed on an FEI Tecnai G2 F20 microscope with a field emission gun operating at 200 kV. Cross-sectional thin lamellae were cut by focused ion beam after the deposition of Pt protective layers, and were subsequently placed onto a Cu TEM grid.

2.4. Defect characterization

Variable energy positron annihilation lifetime spectroscopy (VEPALS) was conducted at the Mono-energetic Positron Source (MePS) beamline at Helmholtz-Zentrum Dresden-Rossendorf (HZDR) in Germany [32,33]. A typical lifetime spectrum $N(t)$ is described by $N(t) = \sum\left(\frac{1}{\tau_i} I_i e^{\left(-\frac{t}{\tau_i}\right)}\right)$, where τ_i and I_i are the positron lifetime and intensity of the ith component, respectively ($\sum I_i = 1$). All the spectra were deconvoluted using a non-linear least-squares fitting method in the frame of the fitting software package PALSfit into 3 discrete lifetime components, [34] which directly evidence localized positron annihilation at 3 different defect types (or sizes: τ_1, τ_2, and τ_3). The corresponding relative intensities reflect, to a large extent, the concentration of each defect type (size) if the size

of compared defects is in a similar range. The positron lifetimes at depths below 20 nm (<2 keV in terms of positron implantation energy, E_P, for both films, might be overestimated due to the influence of roughness and surface broken symmetry, whereas positron lifetimes at further depths are generally directly proportional to defects size, *i.e.*, the larger is the open volume, the lower is the probability and longer it takes for positrons to be annihilated with electrons [35,36]. The positron lifetime and its intensity has been probed in function of positron implantation energy E_P or, in other words, implantation depth (thickness), which is given as mean positron implantation depth: $\langle z \rangle (nm) = \frac{36}{\rho\left(\frac{g}{cm^3}\right)} (E_P(\mathrm{keV})^{1,62})$ [37].

2.5. Ab initio calculations

First-principles calculations are based on the projector-augmented wave (PAW) method [38] as implemented in the Vienna *ab initio* Simulation Package (VASP) [39–41] using the generalized gradient approximation [42]. All fcc and hcp crystal phases of Fe and Co were explored, while a bcc structure was adopted for FeCo alloys that is compatible with the experimental samples. To model FeCo alloys and compare it to bare Co and Fe, we used (2 × 2) supercells with five-monolayer thickness for all structures investigated. The energy barrier an "N" atom needs to overcome in order to be inserted in each surface was evaluated using the nudged elastic band method (NEB) on the nitrogen pathway [43,44]. At each step, the atomic coordinates were relaxed until the forces became as small as 1 meVÅ. A kinetic energy cutoff of 500 eV has been used for the plane-wave basis set and 25 × 25 × 1 *k*-point mesh was used to sample the first Brillouin zone.

3. Results and discussion

3.1. Role of Co:Fe atomic ratio in the magneto-ionics of $Co_{1-x}Fe_xN$ ($0 \leq x < 1$) ternary nitrides

50 nm thick $Co_{1-x}Fe_xN$ ($x = 0.37$, 0.44, 0.51, 0.65, 0.75 and 0.87) ternary nitride films were grown at room temperature by reactive magnetron co-sputtering. The Ti (20 nm) adhesive and Cu (60 nm) seed layers act as working electrode. To serve as a reference, 50 nm CoN (*i.e.*, $x = 0$ in the $Co_{1-x}Fe_xN$ series) films were also deposited. During sputtering, the Ar:N_2 flow ratio was set to 1:1 to prepare nitrogen-rich nitrides with a non-ferromagnetic behavior [24].

To investigate the magneto-ionic performance, vibrating sample magnetometry measurements with in-plane applied magnetic fields were performed at room temperature while the films were gated in a liquid electrolyte. Fig. 1a presents a cartoon of the homemade electrolytic cell used to apply voltage to the nitride films (magneto-ionic targets) in a capacitor-like configuration. Propylene carbonate (PC) with Na^+ and OH^- solvated species was used as the liquid electrolyte. To induce magneto-ionic effects, a bias voltage is applied between the Ti/Cu working electrode and a Pt wire (acting as a counter electrode). When the working electrode is negatively charged, the solvated Na^+ accumulate at the interface with the film, while the PC molecular chains become also oriented with their positive charges facing the nitride film thanks to its dipolar nature. This process, in a realistic scenario, is of course more complex and involves both positive and negative ions, leads to the formation of the so-called "electrical double layer" (EDL), which is an ultra-thin dielectric layer (<1 nm) at the interface, that allows the generation of very strong electric fields (of several MV/cm) for moderate applied voltages as the ones used in the present work [45,46]. Fig. 1b shows the time evolution of the generated magnetization for the series of $Co_{1-x}Fe_xN$ ($0 \leq x < 1$) nitride films electrolyte-gated at −25 V for 20 min. A magnetic field of 10 kOe was applied during these measurements to ensure that the generated ferromagnetic counterparts become magnetically saturated. All as-grown nitride films are virtually non-ferromagnetic, showing $M_S < 10$ emu/cm^3. Once the voltage is applied (at $t = 2$ min), M_S rapidly increases following a rather linear behavior within the first tens of seconds. For longer voltage-actuation time, the generation of magnetization tends to slow down until levelling off for $t > 15$ min, as it usually happens in other magneto-ionic systems, such as Co_3O_4 or CoN [28,47]. The generation of magnetization in response to electrolyte gating is attributed to the EDL charging at the interface and the resulting magneto-ionic effects. Due to the strong electric fields generated at the interface, CoFeN dissociates and N^{3-} are dragged across the film, get redistributed and are partially (or totally) released to the liquid electrolyte [24]. The motion of N^{3-} across the CoFeN films leaves behind clusters of metallic CoFe, which is a ferromagnetic metallic alloy with a high M_S [30]. Our previous studies revealed that, after voltage treatment, depending on the thickness of magneto-ionic layers, the applied voltage strength and the duration of the actuation time, nitrogen-depleted sub-regions form either close to the solid/electrolyte interface (for sufficiently thin nitride layers and fast magneto-ionic responses), deeper inside the films (when the nitride layers are thick and all N^{3-} can be steadily released to the liquid without locally exceeding the solubility limit of nitrogen ions in propylene carbonate), or the whole layer can become metallic, containing no nitrogen at all, if the voltage is applied for sufficiently long times [24,25,28]. While the details of the ion migration mechanism are complex, the basic understanding of this phenomenon is the voltage-driven transformation from CoFeN (paramagnetic at room temperature) to CoFe (ferromagnetic at room temperature). The gradual formation of CoFe gives rise to an increase of magnetization, as depicted in Fig. 1b. Note that, while magneto-ionics is at the heart of the voltage-driven changes of magnetic properties in the studied $Co_{1-x}Fe_xN$ films, some contribution from carrier modulation entangled with N^{3-} migration due to the semiconducting nature of the nitrides, cannot be completely ruled out. Carrier modulation was actually reported to be responsible for the observed changes of Curie temperature and coercivity in (Ga,Mn)As low-temperature magnetic semiconductors as well as in Co-doped titanium dioxide at room temperature [48,49].

The slope of saturation magnetization dependence, dM_S/dt, which is indicative of the speed of the N^{3-} motion, accounts for the magneto-ionic rate and is found to be in the range 3.4–4.3 emu/(cm^3·s). Even though there is no clear trend on the role of Fe content in the magneto-ionic rate, the $Co_{0.35}Fe_{0.65}N$ film shows the largest value (*i.e.*, 4.3 emu/(cm^3·s), as described below), which is the largest nitrogen magneto-ionic rate reported so far for such thickness. Note that in a previous work we showed that electrolyte engineering (*e.g.*, dissolving inorganic salts such as potassium iodide in propylene carbonate electrolyte) can considerably increase the magneto-ionic rate [47]. However, this procedure was detrimental to cyclability. In contrast to the magneto-ionic rate, the steady M_S values (denoted as $M_{S\text{-max}}$) strongly depend on the amount of Fe in the $Co_{1-x}Fe_xN$ nitrides. All ternary films show larger $M_{S\text{-max}}$ values than the binary CoN. This is due, in part, to the larger saturation magnetization of bcc-Fe compared to either fcc- or hcp-Co. Specifically, $M_{S\text{-max}}$ progressively increases with the Fe content up to $x = 0.65$ (reaching 865 emu/cm^3), which is more than twice the value of CoN (425 emu/cm^3). In films with larger Fe contents, $M_{S\text{-max}}$ slightly drops, reaching 790 emu/cm^3 for $x = 0.87$. This resembles, to some extent, the shape of the dependence of M_S with Fe content in $Co_{1-x}Fe_x$ metallic alloys [30,31]. However, the

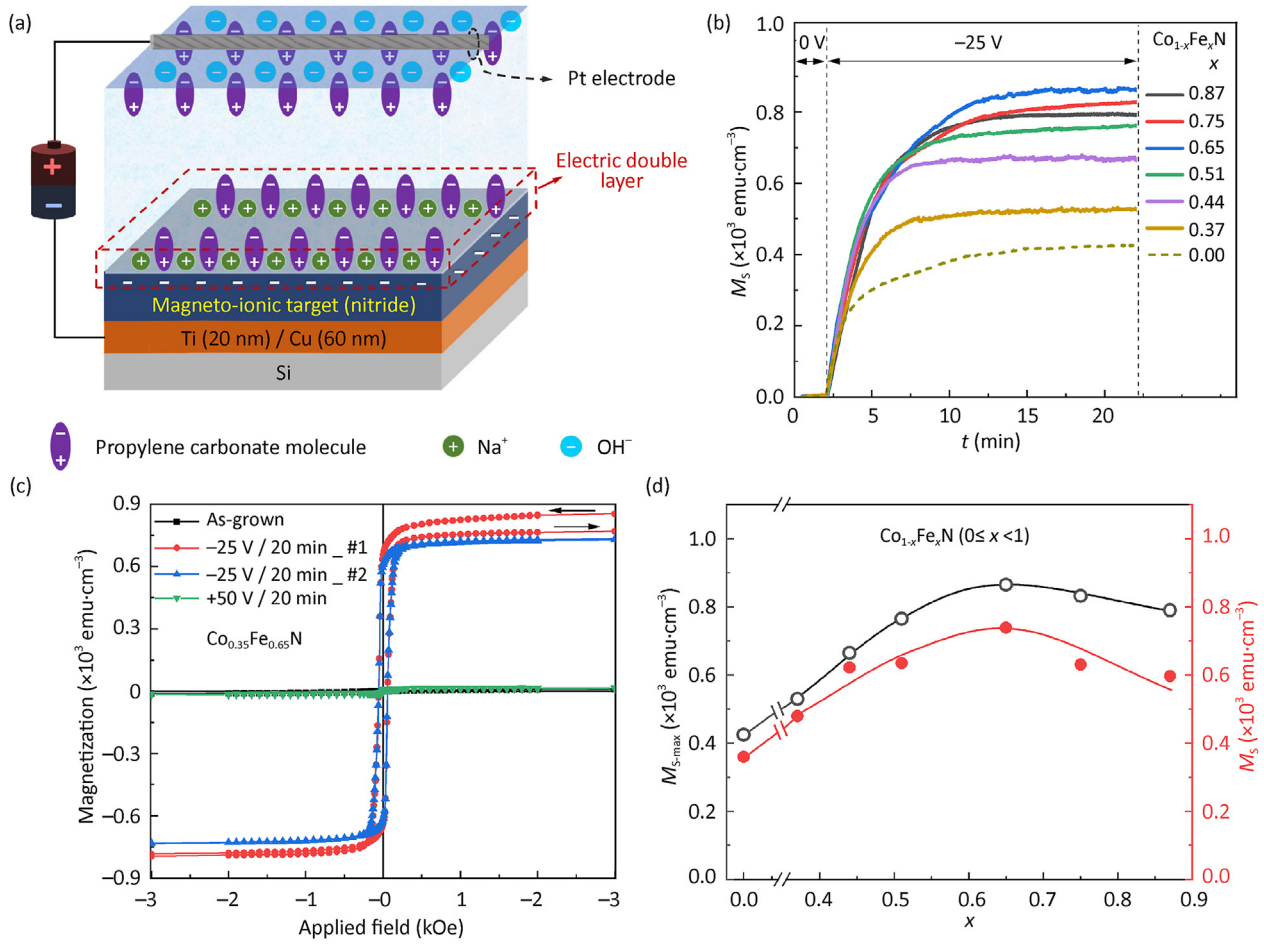

Fig. 1. (a) Schematic illustration of how voltage is applied to the nitride films in the homemade electrolytic cell. (b) Saturation magnetization, M_S, as a function of time, t, for the 50 nm thick $Co_{1-x}Fe_xN$ ($0 \leq x < 1$) ternary nitride films (recorded while applying an external in-plane magnetic field of 10 kOe to ensure saturation of the generated ferromagnetic counterpart). A gating voltage of −25 V was applied at $t = 2$ min for 20 min. (c) Magnetization *vs.* applied magnetic field hysteresis loops recorded before (black) and after (consecutive red and blue loops) voltage actuation for the 50 nm thick $Co_{0.35}Fe_{0.65}N$ nitride film. The black arrows indicate the descending and ascending branches of the first loop taken after switching off the electric field, showing a slight depletion of the generated magnetization. By applying +50 V for 20 min, the virtually non-ferromagnetic state is recovered (green). (d) Evolution with Fe content, x, of the maximum M_S, $M_{S\text{-max}}$ (open black symbols), obtained from the steady-state M_S values in panel (b), and the saturation magnetization, M_S (solid red symbols), of the second hysteresis loops (red) in panel (c) and Fig. S2. The solid lines in (c) and (d) are guides to the eye.

relative changes of M_S with the Fe content in the voltage-actuated magneto-ionic nitride films are more prominent than those in metallic $Co_{1-x}Fe_x$ alloys. For example, while there is a 26 % increase of M_S in $Co_{0.35}Fe_{0.65}$ compared to metallic Co, [30] the attained M_S in voltage-actuated $Co_{0.35}Fe_{0.65}N$ is more than 50% the value of M_S in voltage-actuated CoN. This suggests that the N^{3-} migration mechanism itself has some dependence on the Fe content (probably due to the microstructure evolution when Fe is added to the binary CoN phase).

Fig. 1c shows the hysteresis loops of the as-grown $Co_{0.35}Fe_{0.65}N$ film and the same films treated at the indicated voltage values. The virtual absence of ferromagnetism in the as-grown state (*i.e.*, $M_S < 10$ emu/cm^3) is evident. The very small magnetic signal in the pristine film is likely due to the presence of traces of metallic clusters or contamination in the Si substrate. Remarkably, a clear ferromagnetic hysteresis loop develops after gating it at −25 V for 20 min. As previously reported in other magneto-ionic systems, [21,24] once the voltage is switched off, there is a slight depletion of the generated magnetization (*i.e.*, recovery) during the first recorded measurement (the descending branch of the first hysteresis loop, represented with red symbols, shows a slightly larger M_S than the ascending branch: 854 emu/cm^3 *vs.* 770 emu/cm^3). This effect tends to level off during the second hysteresis loop measurement, represented with blue symbols, which is virtually closed. Subsequently, by subjecting the nitride film to a voltage of 50 V with opposite polarity (*i.e.*, positive) for 20 min, the previously induced magnetization virtually vanishes, recovering the initial paramagnetic state, and thus confirming the magneto-ionic reversibility of the system. Fig. S2 shows analogous hysteresis loops for the other nitride films, according to the measurement protocol followed in Fig. 1c. All hysteresis loops reveal coercivity (H_C) values in the range 30–135 Oe, in agreement with the soft magnetic character of $Co_{1-x}Fe_x$ alloys [30,31]. Fig. 1d depicts the values of $M_{S\text{-max}}$ (black symbols, from the curves in Fig. 1b and M_S (red symbols, obtained after recording the second consecutively measured loop in Fig. 1c and Fig. S2) as a function of the Fe content, x. The difference between both curves accounts for the degree of recovery which tends to be more pronounced for larger Fe contents, envisaging faster magneto-ionic recovery.

3.2. Correlating magneto-ionics with microstructure

Fig. S3 shows the θ–2θ X-ray diffraction patterns of several investigated ternary nitride films and the binary $Co_{0.35}Fe_{0.65}$ alloy. While a clear peak is observed around 44° in $Co_{0.35}Fe_{0.65}$ (which corresponds to the (110) reflection of the bcc phase), in the ternary

nitrides, besides a few peaks from Cu and Si, only a very broad and weak peak is evident in the range between 34° and 36°, indicating that all nitride films are highly nanostructured regardless of composition. This small peak can be attributed to a fcc-(Fe,Co)N phase, consistent with expanded fcc-CoN (111) (JCPDS 00-016-0116), [24] whose expansion could be attributed to nitrogen off-stoichiometries and/or partial Co substitution by Fe. This evidences that the bcc structure of metallic $Co_{0.35}Fe_{0.65}$ cannot hold the large amounts of N incorporated in the films when using sputtering at high N_2 partial pressures, in agreement with previous reports [50]. The result also suggests the possible role of N in stabilizing the fcc structure, as it happens in similar systems [51]. The high nanostructuring degree is likely linked to the use of low voltages during sputtering which tends to result in refined microstructures [52,53]. Upon treatment at −25 V for 20 min, as shown in Fig. S3 for the $Co_{0.35}Fe_{0.65}N$ film, the small peak around 35° vanishes, in agreement with the voltage-induced denitriding process that drives the N^{3-} towards the liquid electrolyte.

To further shed light on the structure of these nitride films, the cross-sections of an as-grown and a voltage-actuated (*i.e.*, −25 V for 20 min) $Co_{0.35}Fe_{0.65}N$ nitride film (the one which shows the highest magneto-ionic rate and the largest generated saturation magnetization among the series) were structurally characterized by high-angle annular dark-field scanning transmission electron microscopy (HAADF-STEM) and high-resolution transmission electron spectroscopy (HRTEM). We also performed compositional characterization using electron energy loss spectroscopy (EELS). Fig. 2a and b present the HAADF-STEM images of the as-grown and treated films together with the Fe, Co and N elemental EELS mappings of the area enclosed within the orange square. In contrast to the pristine film, where homogeneous distributions of Fe, Co and N elements are observed, the treated nitride film shows homogeneous distributions of Fe and Co but an inhomogeneous presence of N, which is mainly located at the top of the film. In fact, two sublayers with dissimilar N content, being the top one richer in N, can be clearly distinguished. This, besides indicating that N^{3-} migration towards the liquid electrolyte takes place in a rather uniform way *via* a planar-like front (in agreement with previously reported results), [24,25] confirms the recently reported effect of N ion accumulation at the interface with the liquid electrolyte (*i.e.*, the top part of the nitride film) for sufficiently fast nitrogen magneto-ionic systems [28]. The observed N^{3-} accumulation stems from the interplay between the high ion motion rates of N^{3-} within the $Co_{0.35}Fe_{0.65}N$ film and the limited sinking capacity of the liquid electrolyte. For slower N^{3-} magneto-ionic systems, depletion of nitrogen is typically observed in the upper part of the films, near the interface with the liquid electrolyte [25]. When magneto-ionic effects are faster (*e.g.*, for very thin CoN, [28] or for the present CoFeN films, as shown here), nitrogen concentration at the interface with the electrolyte is so high that it exceeds the solubility limit of nitrogen in propylene carbonate. In this case, nitrogen remains concentrated at the upper part of the films, being partially released only once voltage has been switched off [28].

This bilayer structure is also ascertained by the normalized EELS line profiles acquired along the film thickness (see Fig. 2c and d). Fig. 2e and f show the HRTEM images and the fast Fourier transforms (FFTs) of the areas enclosed within the orange square of the cross sections of a $Co_{0.35}Fe_{0.65}N$ film before and after electrolyte-

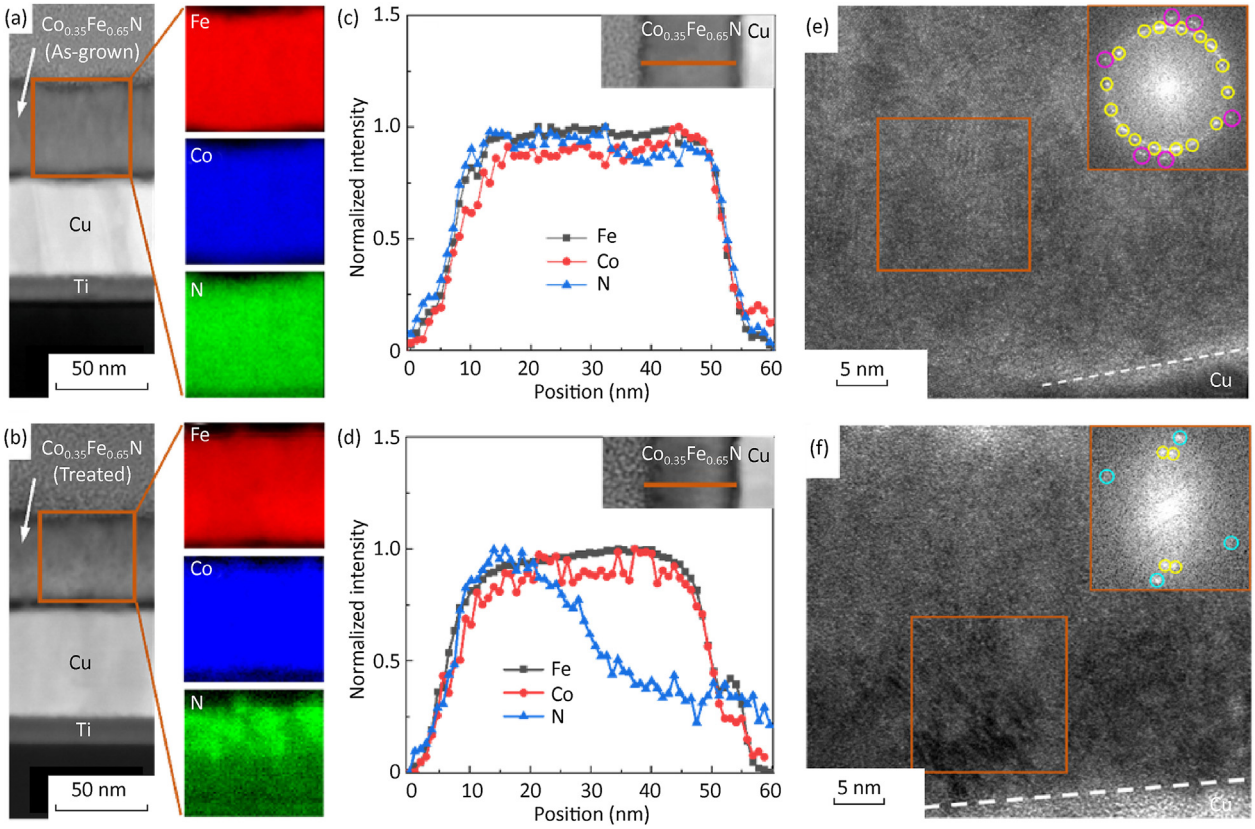

Fig. 2. (a) and (b) show the HAADF-STEM images together with the Fe, Co and N elemental EELS mappings of the area marked with an orange square of a cross-section of as-grown and treated (−25 V for 20 min), respectively, $Co_{0.35}Fe_{0.65}N$ nitrides. (c) and (d) are the normalized concentration depth profiles obtained from EELS. (e) and (f) are the representative HRTEM images of the as-grown and treated (−25 V for 20 min) films, respectively, including the fast Fourier transform of the areas marked with orange squares. The yellow, pink and cyan circles indicate the diffraction spots with interplanar spacing of 2.58, 2.27 Å and 2.05 Å, respectively.

gating at −25 V for 20 min, respectively. The as-grown nitride shows a highly nanocrystalline structure with no well-defined grain boundaries. The FFT shows two sets of discrete spots, corresponding to interplanar distances of 2.58 Å (yellow circles) and 2.27 Å (pink circles). These distances are consistent with (111) and (200) planes of the abovementioned fcc-(Fe,Co)N phase, in concordance with the XRD characterization. For the gated nitride film, the FFT exhibits a lower number of spots, in agreement with a more amorphous-like structure. On top of the (111) reflection spots ascribed to the fcc-(Fe,Co)N phase, additional diffraction spots (cyan circles), corresponding to an interplanar distance of 2.05 Å, appear. These are consistent with the bcc-$Co_{1-x}Fe_x$ (110) reflection, confirming the generation of a ferromagnetic phase by voltage-driven N^{3-} migration. Note that several dark areas appear in the bottom part of the film, which are presumably porous regions formed as a consequence of the removal of nitrogen ions.

Nanostructured films tend to be highly-defective from a structural viewpoint and defects are known to play a central role in ion migration, having a strong impact on the magneto-ionic performance [21,24]. Thus, variable energy positron annihilation lifetime spectroscopy (VEPALS) was carried out to characterize the defect type and density as a function of depth [32–36,54]. With VEPALS, the positron lifetime τ, which is a measure of the defect size and, therefore, of defect type, can be evaluated as a function of depth in the investigated system. In general, three representative size ranges, known as lifetime components τ_i (where $i = 1$, 2 and 3), can be distinguished. The shortest component, τ_1, accounts for vacancy clusters (vacancy agglomerations) inside the grains; the intermediate lifetime component, τ_2, represents larger vacancy clusters linked to grain boundaries, their intersections, or, eventually, small pores in case of $\tau > 500$ ps; finally, the longest lifetime component, τ_3, is associated to the presence of even larger pores or voids. Each component has a corresponding relative intensity (I_i) which, to some extent, reflects the concentration of each defect type [21,24,32–36]. Figs. 3 and 4 show the depth-dependence of τ_1 and τ_2 and the corresponding relative intensities, I_1 and I_2 for the $Co_{0.35}Fe_{0.65}N$ and CoN films before and after voltage actuation (at −25 V for 20 min), respectively. Note that τ_3-associated defects are virtually negligible since the sum of I_1 and I_2 is very close to 100% in all films.

As seen in Fig. 3, at depths above 20 nm, the positron lifetime τ_1 of the as-grown $Co_{0.35}Fe_{0.65}N$ film is significantly larger than that of the binary CoN. A similar trend is also observed for τ_2 (see Fig. 4). Larger defects promote ion diffusion [21,24] and this could help to explain the larger magneto-ionic rate achieved in the ternary nitride. The defect size of the binary CoN is in the range of a four-vacancy complex, [26] hence the as-grown $Co_{0.35}Fe_{0.65}N$ film is expected to have even larger initial open volume. Upon voltage actuation, τ_1 and τ_2 significantly increase as a consequence of the voltage-driven N^{3-} motion. Interestingly, for the $Co_{0.35}Fe_{0.65}N$ film, I_1 reaches almost 100% at the top surface. I_1 tends to decrease with depth, resembling to some extent the N line profile presented in Fig. 2d, becoming a structural fingerprint of the ion accumulation effect. Since I_2 is the complementary parameter to I_1 (*i.e.*, $I_2 = 100\% - I_1$, since $I_3 \approx 0$), I_2 follows an opposite trend, thus being maximum at the bottom of the film. Taking into account that the nitrogen amount in this region is much lower than in the top, N^{3-} motion can somewhat be associated with the formation of larger vacancy clusters linked to grain boundaries or, eventually, small pores. Conversely, for CoN, I_1 significantly increases not only at the surface (spherical vacancy accumulation consisting of about 20 empty sites) but also throughout the layer (about 10 agglomerated vacancies), suggesting that vacancy clusters inside the grains are the dominant defects across the film, evidencing a more restricted ion motion in agreement with the magneto-ionic behavior, which

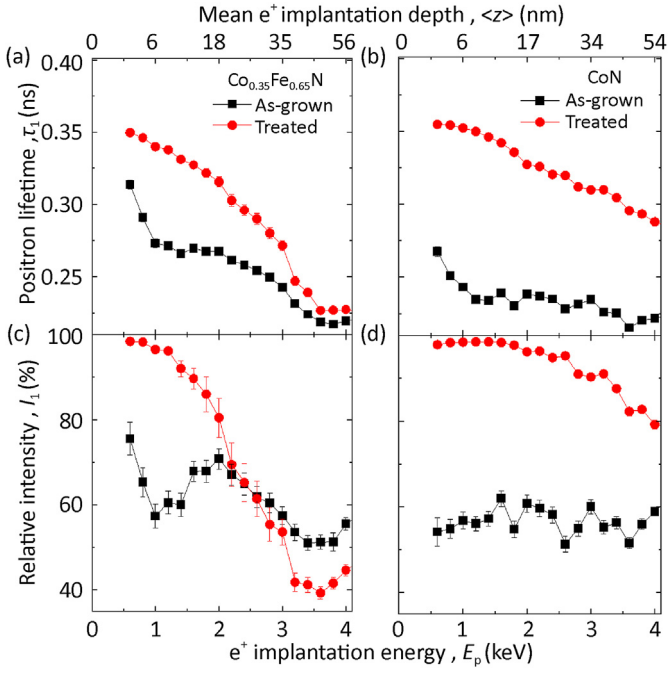

Fig. 3. Depth-resolved defect characterization by VEPALS. (a) and (b) show the positron lifetime component 1 (τ_1) as a function of depth for the 50 nm thick $Co_{0.35}Fe_{0.65}N$ and CoN films, respectively, before (black) and after voltage actuation at −25 V for 20 min (red). (c) and (d) are the corresponding intensities (I_1) as a function of depth for the 50 nm thick $Co_{0.35}Fe_{0.65}N$ and CoN films, respectively, before (black) and after (red) voltage actuation at −25 V for 20 min.

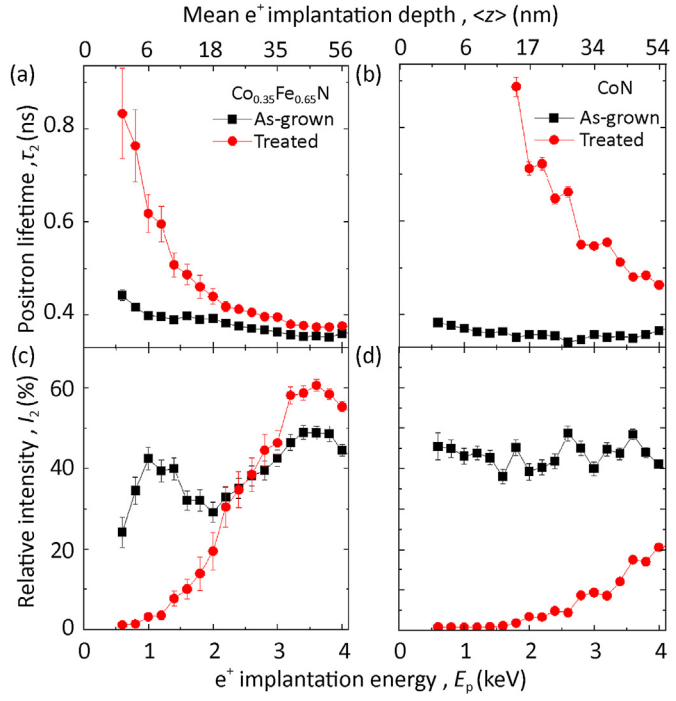

Fig. 4. Depth-resolved defect characterization by VEPALS. (a) and (b) show the positron lifetime component 2 (τ_2) as a function of depth for the 50 nm thick $Co_{0.35}Fe_{0.65}N$ and CoN films, respectively, before (black) and after voltage actuation at −25 V for 20 min (red). (c) and d) are the corresponding intensities (I_2) as a function of depth for the 50 nm thick $Co_{0.35}Fe_{0.65}N$ and CoN films, respectively, before (black) and after (red) voltage actuation at −25 V for 20 min.

shows faster rates for the ternary film. Regardless of composition, the current films outperform, in terms of magneto-ionic rates, the best magneto-ionic results observed so far, achieved in CoN films grown by reactive triode sputtering [28]. For instance, 50 nm thick CoN grown by triode sputtering led to a magneto-ionic rate of 1.8 emu/(cm^3·s), [28] whereas the current CoN film with the same thickness (grown by magnetron sputtering under rather mild power conditions) shows a value close to 4 emu/(cm^3·s). The corresponding τ_1 and τ_2 values (Figs. 3 and 4) are rather similar to those of the CoN grown by triode sputtering [20,24]. However, there are significant differences between the intensities. While I_1 is dominant over I_2 in the triode CoN films, the values of I_1 and I_2 become comparable (being I_1 still slightly larger) in the current as-grown films, indicating that the amount of larger vacancy clusters linked to grain boundaries or, eventually, small pores is larger for our films, in concordance with the higher nanostructuring degree. This would explain, at least partially, the obtained faster rates as a consequence of promoted ion motion in the magnetron sputtered $Co_{0.35}Fe_{0.65}N$ and CoN films.

3.3. Thickness-dependent magneto-ionics in $Co_{0.35}Fe_{0.65}N$ ternary nitride films

Given that the 50 nm $Co_{0.35}Fe_{0.65}N$ film exhibits an improved magneto-ionic response in terms of ion motion rate and amount of generated magnetization, the role of thickness on the magneto-ionic behavior of this particular film composition was also investigated. Films with thickness of 25, 10 nm and 5 nm were grown using the same sputtering conditions. Fig. 5a shows the time-dependent magnetization measurements of the $Co_{0.35}Fe_{0.65}N$ films with thickness of 5, 10, 25 nm and 50 nm, taken while gating the samples at −25 V and applying an external magnetic field of 10 kOe to ensure that the generated ferromagnetic counterpart is always magnetically saturated. Remarkably, both the magneto-ionic motion and the steady saturation magnetization generated after long-term actuation (*i.e.*, $M_{S\text{-max}}$ at $t = 22$ min) increase with the thickness reduction. For instance, after 1 min of voltage actuation, the 5 nm thick film exhibits an M_S value of around 1,000 emu/cm^3, whereas the 50 nm thick shows 260 emu/cm^3 (see Fig. 5b). Moreover, the $M_{S\text{-max}}$ for the thinner film reaches about 1,500 emu/cm^3, which is the largest induced magnetization reported so far for nitrogen magneto-ionics [27,28]. Note that this value is reasonable taking into account that M_S of around 1,850 emu/cm^3 is attained in CoFe alloys with suitable Co:Fe ratio [30]. A strong thickness dependence is also observed in the magneto-ionic rate (Fig. 5c and d). As the film thickness decreases from 50 nm to 5 nm, the maximum slope dM_S/dt during the initial stages of voltage actuation, *i.e.*, the ionic motion rate, increases from 4.3 emu/(cm^3·s) to 35.5 emu/(cm^3·s). The observed maximum ion motion speed represents a 600% improvement compared to the best CoN results reported so far [28]. The dependence of magneto-ionics on film thickness is partially attributed to the fact that thinner films experience an overall stronger electric field strength throughout the whole film thickness under the same applied voltage, thereby larger magnetization is induced. For thicker films, given the semiconducting nature of these nitrides, electric field is very strong at the solid/electrolyte interface, but it decreases towards the interior of the layers. Thus, the overall ion diffusion effects are less pronounced.

3.4. Ab initio calculations: formation energy considerations

The outstanding magneto-ionic performance shown in the previous sections suggests that, besides the aforementioned differences in structural defects, other parameters such as the formation energy of the nitrides, might also play a role in determining

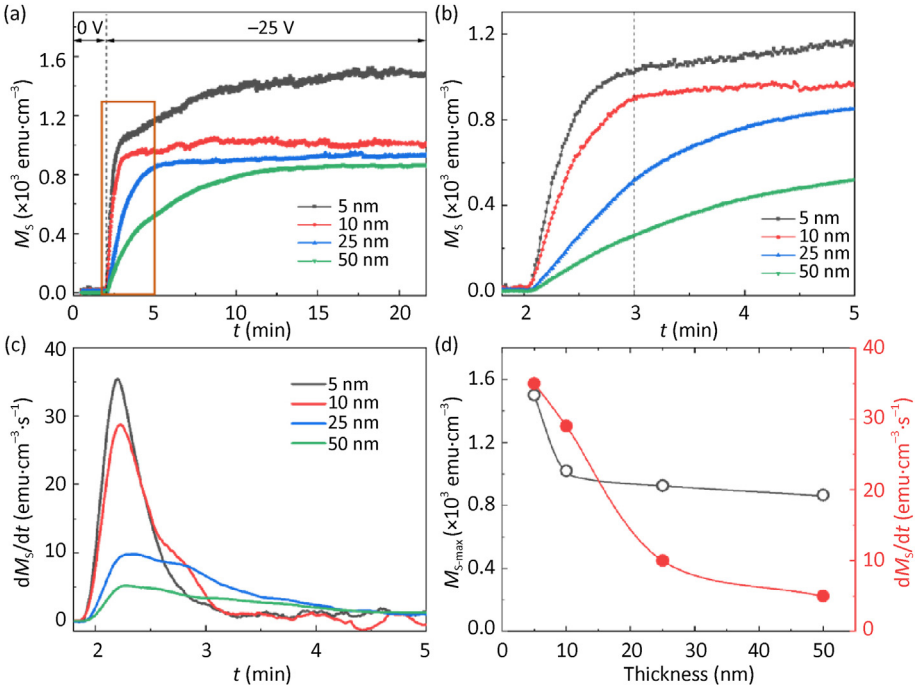

Fig. 5. Thickness-dependent magneto-ionic response in $Co_{0.35}Fe_{0.65}N$ nitride films. (a) Time evolution of the magneto-ionically induced saturation magnetization (M_S) for the $Co_{0.35}Fe_{0.65}N$ nitride films with thickness of 5, 10, 25 nm and 50 nm (recorded while applying an external in-plane magnetic field of 10 kOe). For each film, a gating voltage of −25 V was applied at $t = 2$ min for 20 min. (b) Is the zoom of the area enclosed within the orange rectangle in panel (a). (c) Evolution of the slopes, dM_S/dt, of the initial parts of the curves plotted in panel (a). (d) Thickness dependence of the maximum M_S, $M_{S\text{-max}}$ (open black symbols), taken from panel (a), and the maximum slope presented in panel (c) (solid red symbols). The solid lines in (d) are guides to the eye.

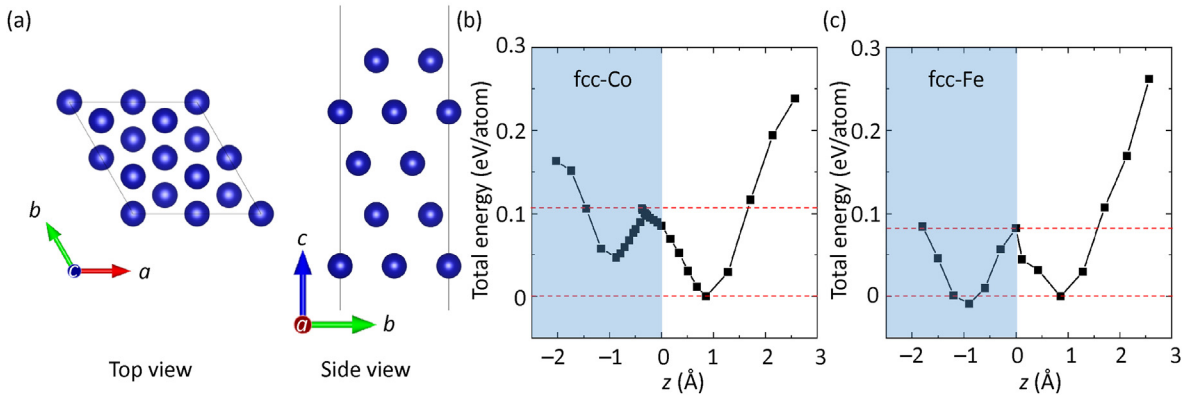

Fig. 6. Calculated total energy per atom, normalized to the minimum energy value, as a function of the displacement between the reference outermost surface atom and the inserted N atom. (a) Schematic of fcc-Co (001) and (100) surfaces, designed for N-atom insertion. (b) and (c) are the energy profiles corresponding to the insertion of a N atom into fcc-Co (111) and fcc-Fe (111) surfaces, respectively.

Table 1
A summary of the calculated energy barriers corresponding to the formation of Co–N and Fe–N bonds when a nitrogen atom is inserted into either fcc or hcp structures in the case of Co and Fe.

Structure	Energy barrier (eV/atom)
fcc-Co	0.10
fcc-Fe	0.08
hcp-Co	0.08
hcp-Fe	0.14
bcc-$Co_{0.35}Fe_{0.65}$	0.06

the fast and strong magneto-ionic response of the $Co_{0.35}Fe_{0.65}N$ films. To investigate this aspect, *ab initio* calculations were performed. The formation energies of Co–N and Fe–N bonds in the different possible crystallographic structures were estimated. As shown in Fig. 6 and Table 1, a lower energy is found for the formation of Fe–N compared to Co–N when a fcc lattice structure is considered. Since $Co_{0.35}Fe_{0.65}N$ consists of a fcc structure (as evidenced by XRD and HRTEM), it can be then understood that the addition of Fe to CoN leads to a lower cohesive energy with weaker bonds with nitrogen. This would promote voltage-driven ion motion. Note that pure FeN is often reported to crystallize in a hexagonal structure [25]. The formation energy in that case is much higher than for the Co or Fe fcc structures (Table 1 and Fig. S4), and this is why magneto-ionic performance of pure FeN is, in fact, worse than for CoN [25].

3.5. Magneto-ionic cyclability in $Co_{0.35}Fe_{0.65}N$

Finally, the magneto-ionic cyclability in $Co_{0.35}Fe_{0.65}N$ films was investigated by subjecting a 10 nm thick $Co_{0.35}Fe_{0.65}N$ film to −8 V/+8 V pulses with a periodicity of 30 s (*i.e.*, 1 min cycle), as shown in Fig. 7. Our X-ray photoelectron spectroscopy indicates that, while a negative voltage applied to the nitride film induces denitriding process due to the transport of N^{3-} toward the electrolyte, N^{3-} are largely restored upon the reversal of gate voltage polarity (see Fig. S5, Supporting Information). This, together with the optimized tradeoff between ion motion rate and signal-to-noise ratio, make the 10 nm nitride film a suitable candidate for cyclability study. Note that a preliminary study revealed that, for this system, magneto-ionics can be induced for gating voltages larger than −4 V, and the induced magnetization scales with the applied voltage (see Fig. S6, Supplementary Information). However, high voltages tend to extract large amounts of N^{3-} from the nitride films during short periods of time. Once dissolved in the propylene carbonate electrolyte, such excess N^{3-} are coulombically attracted towards the counter electrode (which is positively charged), they neutralize and are released from the liquid in the form of N_2 bubbles. Such nitrogen is lost and cannot be reintroduced to the films upon application of positive voltage. On top of this, PC degradation is promoted with voltage, [55] thus hampering N reversibility as well. As shown in Fig. 7, although the amplitude of saturation magnetization, ΔM_S, experiences a slight decrease for long-term voltage actuation, a stable periodic ΔM_S response (above the noise level, see Fig. S7, Supplementary Information) remains even after 1,000 cycles, which is in marked contrast with binary nitrides or ternary CoMnN where endurance is typically no more than a few tens of cycles [24,27]. Besides showing a robust OFF–ON cyclability, the cycles are rather symmetric in shape, indicating an optimal reversibility of N^{3-} motion. Taking into account that metallic $Co_{0.35}Fe_{0.65}$ has a bcc structure, *ab initio* calculations were also performed when a nitrogen ion is inserted into a bcc-$Co_{0.35}Fe_{0.65}$ lattice to estimate the formation energy of CoFe–N. A value of 0.06 eV/atom is found (see Table 1 and Fig. S4, Supplementary Information), which is significantly lower than those of fcc-Co and

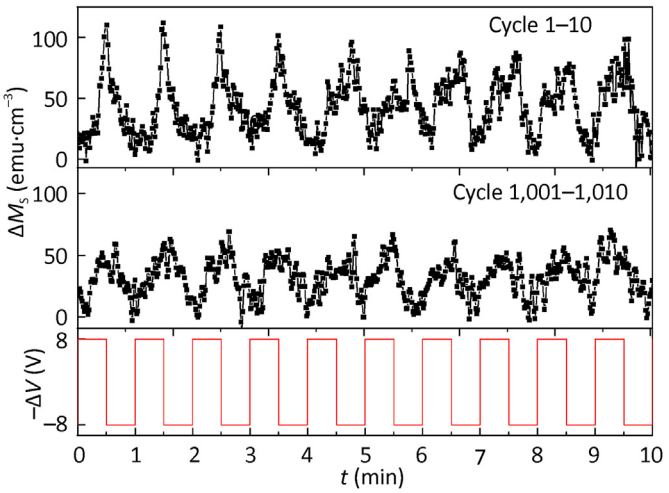

Fig. 7. Magneto-ionic cyclability of a 10 nm thick $Co_{0.35}Fe_{0.65}N$ film subjected to −8 V/+8 V cycles of 1 min of duration. The top and middle panels represent the results of cycle 1–10 and 1,001–1,010, respectively, while the bottom panel depicts the gating voltage cycle, *i.e.*, the time evolution of the voltage stimulus. Note that the magnetic moment change was recorded while applying a magnetic field of 10 kOe so that the generated ferromagnetic counterparts remain always saturated.

fcc-Fe. Even though this is only representative of the initial stages of the reverse process in which N starts to reincorporate into the metallic phase (note that $Co_{0.35}Fe_{0.65}N$ exhibits a fcc structure), the low formation energy of bcc-$Co_{0.35}Fe_{0.65}$ with N would also partly explain the high reversibility and, ultimately, the high cyclability of the $Co_{0.35}Fe_{0.65}N$ films with respect to other systems such as CoN or FeN.

4. Conclusion

In summary, we have investigated the magneto-ionic behavior of $Co_{1-x}Fe_xN$ films as a function of Fe content, x ($0 \leq x < 1$), through electrolyte gating. Paramagnetic and highly nanostructured 50 nm thick $Co_{1-x}Fe_xN$ films (x = 0, 0.37, 0.44, 0.51, 0.65, 0.75 and 0.87) were prepared by reactive co-sputtering. These films show magneto-ionic rates at early stages of voltage actuation of up to 4.3 emu/($cm^3 \cdot s$), which are the fastest reported so far in N^{3-} magneto-ionics for this film thickness. The incorporation of Fe also results in a significant increase in the steady magnetization induced by magneto-ionics, which is linked, in part, to the larger saturation magnetization of bcc-Fe compared to either fcc- or hcp-Co. Other effects, such as the dissimilar types and increased sizes of vacancy defects in the as-grown ternary films compared to the binary nitride films (as revealed by positron annihilation spectroscopy), as well as the differences in formation energies between Fe–N and Co–N in the different crystallographic structures (studied by *ab initio* calculations), are found to contribute to the improved magneto-ionic performance in $Co_{1-x}Fe_xN$ compared to CoN. Remarkably, magneto-ionic rates and induced magnetization can be significantly enhanced further by decreasing the $Co_{1-x}Fe_xN$ film thickness. A magneto-ionic rate as high as 35.5 emu/($cm^3 \cdot s$) is achieved for 5 nm thick films. Finally, the endurance of the ternary $Co_{1-x}Fe_xN$ films is drastically improved (up to > 1,000 cycles) compared to binary nitrides. The results presented here are highly relevant for the further exploitation of nitrogen magneto-ionics in forthcoming technological applications.

Data availability

Data will be made available on request.

Declaration of competing interest

The authors declare that they have no known competing financial interests or personal relationships that could have appeared to influence the work reported in this paper.

Acknowledgements

Financial support by the European Union's Horizon 2020 Research and Innovation Programme (BeMAGIC European Training Network, ETN/ITN Marie Skłodowska–Curie grant Nº 861145), the European Research Council (2021-ERC-Advanced REMINDS Grant Nº 101054687), the Spanish Government (PID2020-116844RBeC21, TED2021-130453B-C22 and PDC2021-121276-C31) and the Generalitat de Catalunya (2021-SGR-00651) and the MCIN/AEI/10.13039/501100011033 & "European Union NextGenerationEU/PRTR" (grant CNS2022-135230) is acknowledged. VEPALS was carried out at ELBE from the Helmholtz-Zentrum Dresden-Rossendorf e. V., a member of the Helmholtz Association. We would like to thank the facility staff for assistance. This work was partially supported by the Impulse-und Net-working fund of the Helmholtz Association (FKZ VH-VI-442 Memriox), and the Helmholtz Energy Materials Characterization Platform (03ET7015). E. M. is a Serra Húnter Fellow.

Appendix A. Supplementary data

Supplementary data to this article can be found online at https://doi.org/10.1016/j.jmat.2023.10.007.

References

[1] Bandyopadhyay S, Atulasimha J, Barman A. Magnetic straintronics: manipulating the magnetization of magnetostrictive nanomagnets with strain for energy-efficient applications. Appl Phys Rev 2021;8:041323.
[2] Sun F, Chen D, Gao X, Liu JM. Emergent strain engineering of multiferroic $BiFeO_3$ thin films. J Materiomics 2021;7:281.
[3] Kirilyuk A, Kimel AV, Rev Rasing T. Ultrafast optical manipulation of magnetic order. Rev Mod Phys 2010;82:2731.
[4] Vergès M, Perumbilavil S, Hohlfeld J, Freire-Fernández F, Guen YL, Kuznetsov N, et al. Energy efficient single pulse switching of $[Co/Gd/Pt]_N$ nanodisks using surface lattice resonances. Adv Sci 2023;10:2204683.
[5] Ramesh R, Manipatruni S. Electric field control of magnetism. Proc R Soc A 2021;477:20200942.
[6] Song C, Cui B, Li F, Zhou X, Pan F. Recent progress in voltage control of magnetism: materials, mechanisms, and performance. Prog Mater Sci 2017;87:33.
[7] Hu JM, Nan CW. Opportunities and challenges for magnetoelectric devices. Apl Mater 2019;7:080905.
[8] Molinari A, Hahn H, Kruk R. Voltage-control of magnetism in all-solid-state and solid/liquid magnetoelectric composites. Adv Mater 2019;31:1806662.
[9] Nichterwitz M, Honnali S, Kutuzau M, Guo S, Zehner J, Nielsch K. Advances in magneto-ionic materials and perspectives for their application. Apl Mater 2021;9:030903.
[10] Jensen CJ, Quintana A, Quarterman P, Grutter AJ, Balakrishnan PP, Zhang H, et al. Nitrogen-based magneto-ionic manipulation of exchange bias in CoFe/MnN heterostructures. ACS Nano 2023;17:6745.
[11] Wang Q, Gu Y, Chen C, Pan F, Song C. Oxide spintronics as a knot of physics and chemistry: recent progress and opportunities. J Phys Chem Lett 2022;13(43):10065.
[12] Tan AJ, Huang M, Avci CO, Büttner F, Mann M, Hu W, et al. Magneto-ionic control of magnetism using a solid-state proton pump. Nat Mater 2019;18:35.
[13] Gößler M, Albu M, Klinser G, Steyskal EM, Krenn H, Würschum R. Magneto-ionic switching of superparamagnetism. Small 2019;15:1904523.
[14] Chen G, Ophus C, Quintana A, Kwon H, Won C, Ding H, et al. Reversible writing/deleting of magnetic skyrmions through hydrogen adsorption/desorption. Nat Commun 2022;13:1350.
[15] Lu N, Zhang Z, Wang Y, Li HB, Qiao S, Zhao B, et al. Enhanced low-temperature proton conductivity in hydrogen-intercalated brownmillerite oxide. Nat Energy 2022;7:1208.
[16] Dasgupta S, Das B, Knapp M, Brand RA, Ehrenberg H, Kruk R, et al. Intercalation-driven reversible control of magnetism in bulk ferromagnets. Adv Mater 2014;26:4639.
[17] Dasgupta S, Das B, Li Q, Wang D, Baby TT, Indris S, et al. Toward on-and-off magnetism: reversible electrochemistry to control magnetic phase transitions in spinel ferrites. Adv Funct Mater 2016;26:7507.
[18] Zhu X, Zhou J, Chen L, Guo S, Liu G, Li RW, et al. In situ nanoscale electric field control of magnetism by nanoionics. Adv Mater 2016;28:7658.
[19] Bauer U, Yao L, Tan AJ, Agrawal P, Emori S, Tuller HL, et al. Magneto-ionic control of interfacial magnetism. Nat Mater 2015;14:174.
[20] Gilbert DA, Grutter AJ, Arenholz E, Liu K, Kirby BJ, Borchers JA, et al. Structural and magnetic depth profiles of magneto-ionic heterostructures beyond the interface limit. Nat Commun 2016;7:12264.
[21] Quintana A, Menéndez E, Liedke MO, Butterling M, Wagner A, Sireus V, et al. Voltage-controlled ON–OFF ferromagnetism at room temperature in a single metal oxide film. ACS Nano 2018;12:10291.
[22] Chen Z, Sun H, Zhou X, Duan H, Yan W, Yin Y, et al. Continuous and fast magneto-ionic control of magnetism in $Ta/Co/BiFeO_3/SrRuO_3$ multiferroic heterostructure. J. Materiomics. 2022;8:1141.
[23] Tan Z, Ma Z, Fuentes L, Liedke MO, Butterling M, Attallah AG, et al. Regulating oxygen ion transport at the nanoscale to enable highly cyclable magneto-ionic control of magnetism. ACS Nano 2023;17:6973.
[24] de Rojas J, Quintana A, Lopeandía A, Salguero J, Muñiz B, Ibrahim F, et al. Voltage-driven motion of nitrogen ions: a new paradigm for magneto-ionics. Nat Commun 2020;11:5871.
[25] de Rojas J, Salguero J, Ibrahim F, Chshiev M, Quintana A, Lopeandia A, et al. Magneto-ionics in single-layer transition metal nitrides. ACS Appl Mater Interfaces 2021;13:30826.
[26] de Rojas J, Salguero J, Quintana A, Lopeandia A, Liedke MO, Butterling M, et al. Critical role of electrical resistivity in magnetoionics. Phys Rev Appl 2021;16:034042.
[27] Tan Z, Martins S, Escobar M, de Rojas J, Ibrahim F, Chshiev M, et al. From binary to ternary transition-metal nitrides: a boost toward nitrogen magneto-ionics. ACS Appl Mater Interfaces 2022;14:44581.
[28] Tan Z, de Rojas J, Martins S, Lopeandia A, Quintana A, Cialone M, et al. Frequency-dependent stimulated and post-stimulated voltage control of magnetism in transition metal nitrides: towards brain-inspired magneto-ionics. Mater Horiz 2023;10:88.

[29] Cable JW, Tsunoda Y. Magnetic moments and short-range order in CoMn and NiMn alloys. J Magn Magn Mater 1995;93:140.
[30] Scheunert G, Heinonen O, Hardeman R, Lapicki A, Gubbins M, Bowman RM. A review of high magnetic moment thin films for microscale and nanotechnology applications. Appl Phys Rev 2016;3:011301.
[31] Inturi V, Yin H, Kief M, Hadley M, Mathieu C. Practical FeCo films for perpendicular writer pole. IEEE Trans Magn 2012;48:1718.
[32] Wagner A, Butterling M, Liedke MO, Potzger K, Krause-Rehberg R. Positron annihilation lifetime and Doppler broadening spectroscopy at the ELBE facility. AIP Conf Proc 2018;1970:040003.
[33] Hirschmann E, Butterling M, Hernandez Acosta U, Liedke MO, Attallah AG, Petring P, et al. A new system for real-time data acquisition and pulse parameterization for digital positron annihilation lifetime spectrometers with high repetition rates. J Instrum 2021;16:P08001.
[34] Olsen JV, Kirkegaard P, Pedersen NJ, Eldrup M. PALSfit: a new program for the evaluation of positron lifetime spectra. Phys Status Solidi 2007;4:4004.
[35] Krause-Rehberg R, Leipner HS. Positron annihilation in semiconductors: defect studies. Berlin Heidelberg, New York: Springer-Verlag; 1999.
[36] Tuomisto F, Makkonen I. Defect identification in semiconductors with positron annihilation: experiment and theory. Rev Mod Phys 2013;85:1583.
[37] Liedke MO, Anwand W, Bali R, Cornelius S, Butterling M, Trinh TT, et al. Open volume defects and magnetic phase transition in Fe60Al40 transition metal aluminide. J Appl Phys 2015;117:163908.
[38] Blöchl PE. Projector augmented-wave method. Phys Rev B 1994;50:17953.
[39] Kresse G, Hafner J. Ab initio molecular dynamics for liquid metals. Phys Rev B 1993;47:558.
[40] Kresse G, Furthmüller J. Efficient iterative schemes for ab initio total-energy calculations using a plane-wave basis set. Phys Rev B 1996;54:11169.
[41] Kresse G, Furthmüller. Efficiency of ab-initio total energy calculations for metals and semiconductors using a plane-wave basis set. J Comput Mater Sci 1996;6:15.
[42] Perdew JP, Burke K, Ernzerhof M. Generalized gradient approximation made simple. Phys Rev Lett 1996;77:3865.
[43] Henkelman G, Uberuaga BP, Jónsson H. A climbing image nudged elastic band method for finding saddle points and minimum energy paths. J Chem Phys 2000;113:9901.
[44] Henkelman G, Jónsson H. Improved tangent estimate in the nudged elastic band method for finding minimum energy paths and saddle points. J Chem Phys 2000;113:9978.
[45] Leighton C. Electrolyte-based ionic control of functional oxides. Nat Mater 2019;18:13.
[46] Navarro-Senent C, Quintana A, Menéndez E, Pellicer E, Sort J. Electrolyte-gated magnetoelectric actuation: phenomenology, materials, mechanisms, and prospective applications. Apl Mater 2019;7:030701.
[47] Martins S, Ma Z, Solans-Monfort X, Sodupe M, Rodriguez-Santiago L, Menéndez E, et al. Enhancing magneto-ionic effects in cobalt oxide films by electrolyte engineering. Nanoscale Horiz 2023;8:118.
[48] Stolichnov I, Riester SWE, Trodahl HJ, Setter N, Rushforth AW, Edmonds KW, et al. Non-volatile ferroelectric control of ferromagnetism in (Ga,Mn)As. Nat Mater 2008;7:464.
[49] Yamada Y, Ueno K, Fukumura T, Yuan HT, Shimotani H, Iwasa Y, et al. Electrically induced ferromagnetism at room temperature in cobalt-doped titanium dioxide. Science 2011;332:1065.
[50] Sun NX, Wang SX, Hung CY, Chien CX, Tong HC. Microstructures and soft magnetic properties of high saturation magnetization Fe-Co-N alloy thin films. Mater Res Soc Symp Proc 2000;614. F9.2.1.
[51] Hasegawa T, Shirai C, Takemasa Y, Seki Y. TEM observation of nitrogen-tunable bcc–bct–fcc transformation of iron-cobalt with added vanadium. AIP Adv 2020;10:015110.
[52] Vashaei Z, Aikawa T, Ohtsuka M, Kobatake H, Fukuyama H, Ikeda S, et al. Influence of sputtering parameters on the crystallinity and crystal orientation of AlN layers deposited by RF sputtering using the AlN target. J Cryst Growth 2009;311:459.
[53] Kosarian A, Shakiba M, Farshidi E. Role of sputtering power on the microstructural and electro-optical properties of ITO thin films deposited using DC sputtering technique. IEEJ Trans Electr Electron Eng 2018;13:27.
[54] Schultz PJ, Lynn KG. Interaction of positron beams with surfaces, thin films, and interfaces. Rev Mod Phys 1988;60:701.
[55] Eichinger G. Cathodic decomposition reactions of propylene carbonate. J Electroanal Chem Interfacial Electrochem 1976;74:183.

Zheng Ma received his Ph.D. degree in Materials Science in 2021 from the Institute of Materials Science of Barcelona (ICMAB-CSIC), where he worked on magnetic and multiferroic nanoparticles and thin films, exploiting a wide range of experimental techniques (both advanced lab equipment and large-scale facilities). He is now a postdoctoral researcher in Gnm^3 group at Universitat Autònoma de Barcelona (UAB). His current research activities deal with voltage control of magnetism via especially magneto-ionics in transition-metal oxide or nitride thin films, using a liquid or solid electrolyte.

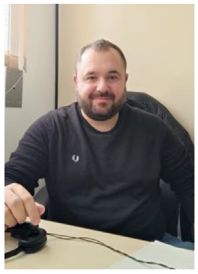

Enric Menéndez is currently a Serra Húnter tenure-track professor in Applied Physics at Universitat Autònoma de Barcelona (UAB). In 2008, he obtained his Ph.D. degree in Materials Science from UAB. He spent 1 year at the Institute of Ion Beam Physics and Materials Research (Helmholtz-Zentrum Dresden-Rossendorf, Germany) and 6 years at the Institute for Nuclear and Radiation Physics (KU Leuven, Belgium), where he built a broad background in Applied Physics and Materials Science, particularly in the cross-fertilization of ion beam modification of materials and magnetism. His mid-to-long term research interests tackle voltage (electric-field) control of magnetism and, in particular, magneto-ionics, which refers to voltage-induced ion migration phenomena to modify magnetic properties, for secure and energy-efficient spintronics and neuromorphics.

Jordi Sort leads the “Group of Smart Nanoengineered Materials, Nanomechanics and Nanomagnetism (Gnm^3)” as an ICREA Research Professor at Universitat Autònoma de Barcelona. After finishing his Ph.D. degree in 2002, Prof. Sort performed two postdoctoral stays, at SPINTEC (Grenoble) and at Argonne National Laboratory. His research is focused on a wide variety of materials (thin films, lithographed structures, porous materials and nanocomposites) with emphasis on their magnetic, magnetoelectric and mechanical performance. He has published around 355 articles that have received over 11,000 citations (h = 53) in ISI Web of Science. He received awards from the Catalan and Spanish Physical Societies as well as the Federation of European Materials Societies, and has managed 38 research projects, being Coordinator of 2 European Training Networks (ITN), and PI of a CoG, a PoC and an AdG from the ERC.